MATERIALS CHEMISTRY FRONTIERS

CCS 中国化学会 CHINESE CHEMICAL SOCIETY

ICCAS

ROYAL SOCIETY OF CHEMISTRY

Near-infrared Electron Acceptors with Fused Nonacyclic Molecular Backbones for Nonfullerene Organic Solar Cells

Journal:	*Materials Chemistry Frontiers*
Manuscript ID	QM-RES-12-2019-000754.R1
Article Type:	Research Article
Date Submitted by the Author:	12-Feb-2020
Complete List of Authors:	Zhang, Jianquan; Hong Kong University of Science and Technology Li, Yunke; The Hong Kong University of Science and Technology, Department of Chemistry Peng, Zhengxing; North Carolina State University Bai, Fujin; The Hong Kong University of Science and Technology, Department of Chemistry Ma, Lik Kuen; The Hong Kong University of Science and Technology, Chemistry Ade, Harald; North Carolina State University, Department of Physics Li, Zhengke; Sun Yat-sen University, Materials Science and Engineering Yan, He; The Hong Kong University of Science and Technology, Department of Chemistry

Near-infrared Electron Acceptors with Fused Nonacyclic Molecular Backbones for Nonfullerene Organic Solar Cells

Jianquan Zhang,‡[ab] Yunke Li,‡[b] Zhengxing Peng,‡[d] Fujin Bai,[b] Lik-Kuen Ma,[b] Harald Ade,*[d] Zhengke Li,*[a] He Yan*[bc]

[a] Key Laboratory for Polymeric Composite and Functional Materials of Ministry of Education, School of Materials and Engineering, Sun Yet-Sen University, Guangzhou 510275, China

[b] Department of Chemistry, Hong Kong University of Science and Technology (HKUST), Clear Water Bay, Kowloon, Hong Kong SAR, P. R. China

[c] Hong Kong University of Science and Technology-Shenzhen Research Institute, No. 9, Yuexing 1st RD, Hi-tech Park, Nanshan, Shenzhen 518057, P. R. China

[d] Department of Physics and Organic and Carbon Electronics Laboratory, North Carolina State University, Raleigh, North Carolina 27695, United States

‡ These authors contributed equally to this work.

Corresponding Author

He Yan: hyan@ust.hk

Zhengke Li: lizhengke@mail.sysu.edu.cn

Harald Ade: harald_ade@ncsu.edu

Abstract

Core engineering of small molecule acceptors (SMAs) is crucially important for enhancing device efficiency for nonfullerene organic solar cells (NF-OSCs). The most commonly used SMAs (e.g., ITIC) utilize indacenodithieno[3,2-b]thiophene (IDTT) as the central core, which has restricted their absorption ranges due to the weak electron-donating ability and short conjugation length. Here, we fused two electron-rich units, namely cyclopenta[2,1-b:3,4-b']dithiophene (CPDT) and dithieno[3,2-b:2',3'-d]pyran (DTPR), into the cores for constructing low-bandgap SMAs. The resulting CPDT-4Cl and DTPR-4Cl molecules exhibit extended nonacyclic central cores and strengthened intramolecular transfer (ICT) effect, resulting in red-shifted absorption (up to ~950 nm) and up-shifted HOMO levels compared with IDTT-4Cl. Consequently, the NF-OSCs based on PTB7-Th:CPDT-4Cl and PTB7-Th:DTPR-4Cl achieved higher PCEs of 12.15% and 10.75%, respectively, than those of the PTB7-Th:IDTT-4Cl ones (7.70%). Notably, high short-circuit current densities (J_{SC}) of 23-25 mA/cm^2 were obtained by the CPDT-4Cl and DTPR-4Cl-based devices, indicating the great potential of the electron-donating CPDT and DTPR as promising building blocks to construct high-performance low-bandgap SMAs.

1. Introduction

The invention of novel organic semiconducting materials has propelled the field of organic photovoltaics and the development of light-weight, inexpensive, solution-processable and roll-to-roll compatible organic solar cells (OSCs). Extensive efforts have been devoted to the development of small molecular acceptor (SMA)-based OSCs, since SMAs possess advantages such as facile synthesis, tunable optical absorption and energy levels, and potentially good device stability.[1-5] The best-performing SMAs typically feature the A-D-A structure, which consists of a multicyclic aromatic core as the electron-donating part and two terminal groups as the electron-withdrawing part.[6-9] The manipulation of the intramolecular charge transfer (ICT) effect between the electron-donating and electron-withdrawing units can easily fine-tune the absorption spectra as well as energy levels of A-D-A-type SMAs. Although the most popular A-D-A-type SMAs based on indacenodithieno[3,2-b]thiophene (IDTT), IT-4F or IT-4Cl, have boosted the power conversion efficiencies (PCE) surpassing 14%,[10-13] the IDTT central core exhibits relatively short conjugated length and weak electron-donating ability, leading to limited absorption ranges of the resulting SMAs (generally with absorption onset of <850 nm).[14-20]

As a large portion of solar energy is distributed in the near-infrared (NIR) region, the development of SMAs with strong NIR photon response is of great importance to harvest the full potential of photons and further improve the short-circuit current density (J_{SC}) and PCEs of non-fullerene OSCs. Moreover, NIR-absorbing SMAs are indispensable for the fabrication of efficient semi-transparent,[21-23] tandem,[24-27] or ternary OSC devices[28-31]. Synthetic strategies have been recently proposed to construct NIR-absorbing SMAs with absorption onset beyond 900 nm, such as the introduction of oxygen or nitrogen atoms, [23, 32-36] extension of the conjugated systems,[37, 38] quinoid-resonance effects,[39, 40] and replacement of benzene with thieno[3,2]thiophene.[21, 41] In addition, there are a large amount of electron-donating building blocks that are

originally used in the synthesis of low-bandgap materials for optoelectronic applications, which remains unexplored for constructing low-bandgap SMAs.[42] Among these building blocks, cyclopenta[2,1-b:3,4-b']dithiophene (CPDT) and dithieno[3,2-b:2',3'-d]pyran (DTPR), originally utilized for tandem OSC applications,[43-45] feature strong electron-donating ability and relatively easy synthesis, and have the ability to extend the absorption range of SMAs to beyond 900 nm.[46-48] Especially, the DTPR unit having one more oxygen atom compared with the CPDT one possesses even stronger electron-donating ability, which is reflected by the up-shifted HOMO levels as indicated by calculations (**Figure 1a**). Moreover, the sp^3-hybridized carbon atoms with additional alkyl chains of CPDT and DTPR prevent excessive intermolecular aggregation and thus render decent solubility of the resulting SMAs.

Herein, we demonstrate the fusion of CPDT and DTPR into the IDTT-like molecular backbone to yield two electron acceptors, CPDT-4Cl and DTPR-4Cl (**Figure 1b**), for OSC operations. Owing to the enhanced ICT effect and the extended nonacyclic central core, the resulting CPDT-4Cl and DTPR-4Cl exhibit dramatically red-shifted (up to ~950 nm) and more intense absorption compared with IDTT-4Cl, as predicted by theoretical calculations. In addition, both HOMO and LUMO levels of CPDT-4Cl and DTPR-4Cl are elevated relative to IDTT-4Cl. In OSC devices consisting of PTB7-Th (**Figure 1c**) as the donor polymer, the CPDT-4Cl-based cells show the highest PCE of 12.15% with an open-circuit voltage (V_{OC}) of 0.74 V, a J_{SC} of 23.24 mA cm^{-2} and an FF of 69.1%, which outperforms the IDTT-4Cl-based ones with the highest PCE of 7.70% with a V_{OC} of 0.61 V, a J_{SC} of 18.34 mA cm^{-2} and an FF of 64.3%. Besides, the further extended absorption of DTPR-4Cl enables an even higher J_{SC} of 24.97 mA cm^{-2}, but an inferior FF of 61.8% leads to a moderate PCE of 10.75%. Morphology studies reveal that the PTB7-Th:CPDT-4Cl blend exhibits suitable phase separation relative to the other two systems, leading to suppressed charge recombination and thereby accounting for its superior device performances.

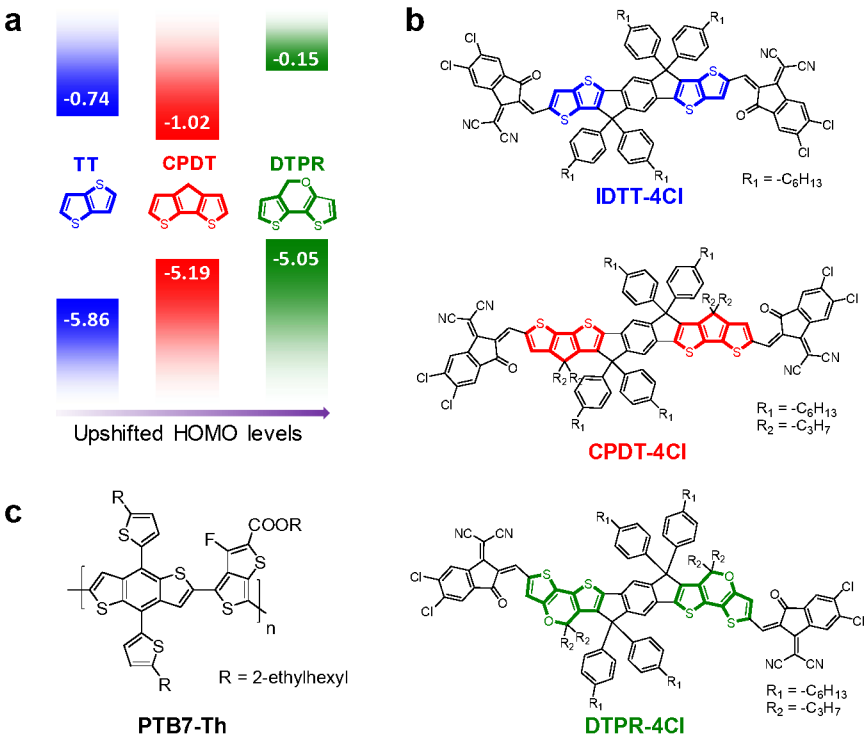

Figure 1. (a) Energy diagram of thieno[3,2-b]thiophene (TT), cyclopenta[2,1-b:3,4-b']dithiophene (CPDT) and dithieno[3,2-b:2',3'-d]pyran (DTPR). (b) Chemical structure of IDTT-4Cl and CPDT-4Cl and DTPR-4Cl. (c) Chemical structure of the donor polymer, PTB7-Th.

2. Results and Discussions

The synthetic route to CPDT-4Cl and DTPR-4Cl is illustrated in **Scheme 1**, which is very similar to that of IDTT-4Cl. Starting from commercially available diethyl 2,5-dibromoterephthalate, the two central cores were readily prepared via a three-step procedure, i.e., palladium-catalyzed Stille or Suzuki cross-coupling, substitution by alkyl phenyl side chains, and acid-assisted Friedel-Crafts intramolecular cyclization in decent yields. After the Vilsmeier-Haack reactions, the resulting dialdehyde compounds underwent the Knoevenagel condensation with the end group, 2-(5,6-dichloro-3-oxo-2,3-dihydro-1H-inden-1-ylidene)malononitrile (IC-2Cl) to yield the targeted SMAs, CPDT-4Cl and DTPR-4Cl. Both molecules were unambiguously characterized by ^{1}H NMR, ^{13}C NMR and mass spectra, which are summarized in the

Supporting Information. The thermal decomposition temperature (T_d) at 5% weight loss of IDTT-4Cl, CPDT-4Cl and DTPR-4Cl were determined to be 375, 383 and 353 °C, respectively, suggesting their good thermal stability (**Figure S1**).

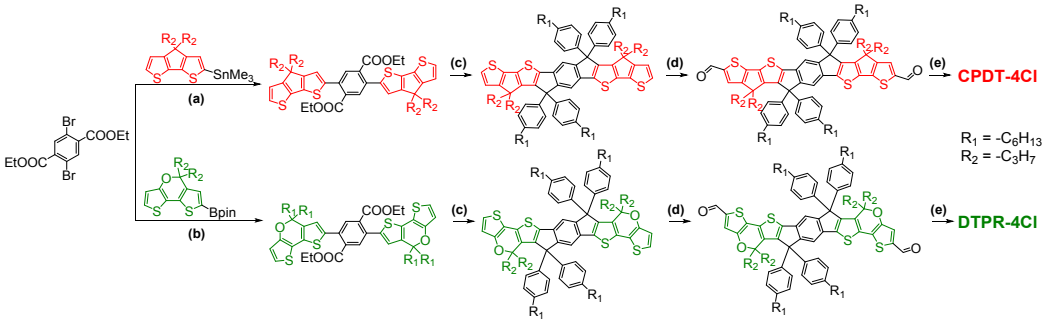

Scheme 1. Synthesis route to CPDT-4Cl and DTPR-4Cl. Reaction conditions: **a.** $Pd_2(dba)_3$, P(*o*-tol)$_3$, toluene, 110 °C; **b.** $Pd(dppf)Cl_2$, K_2CO_3, 1,4-dioxane/H_2O (4:1), 100 °C; **c.** i) 4-bromo-hexylbenzene, *n*-BuLi, THF, -78 °C; ii) octane, conc. H_2SO_4, AcOH, r.t.; **d.** $POCl_3$, DMF, 1,2-dichloroethane, 85 °C; **e**. IC-2Cl, $CHCl_3$, pyridine, 65 °C.

Theoretical calculations were performed using density-functional theory (DFT) with B3LYP/6-31(d,p) basis set to investigate the effects of the core variations on the molecular geometries and electronic properties of IDTT-4Cl, CPDT-4Cl and DTPR-4Cl. The alkyl chains were replaced by methyl groups for simplification. As shown in **Figure 2**, the optimized geometries of IDTT-4Cl and CPDT-4Cl are highly planar with very small S-C-C-S dihedral angles of <1° owing to the planar structure of TT and CPDT. In contrast, the non-planar nature of the six-member ring of DTPR (O-C-C-S dihedral angle of 13.0°) causes two changes in the molecular geometry of DTPR-4Cl. On the one hand, it is observed from the front view that the planarity of the DTPR-4Cl molecule is not as high as the other two, which may reduce the tendency of intermolecular π-π stacking. It is also demonstrated in previous literature that after the introduction of the oxygen atom, it endows better solubility for the DTPR-based polymers than the CPDT-based ones.[43] On the other hand, from the top view DTPR-

4Cl shows a wavier backbone with an angle of 66.7° between the core and the end groups than IDTT-4Cl (49.8°) and CPDT-4Cl (53.6°). Regarding the frontier molecular orbitals (FMO), the HOMO levels are gradually upshifted from -5.65 to -5.33 and to -5.29 eV for IDTT-4Cl, CPDT-4Cl and DTPR-4Cl, respectively, which is consistent with the trend of the upshifted HOMO levels of the corresponding building blocks (**Figure 1a**). Further theoretical calculations using time-dependent DFT (TDDFT) were conducted to compare the optical absorption of three SMAs shown in **Figure S2a**. The main absorption peaks are located at 667, 726 and 772 nm for IDTT-4Cl, CPDT-4Cl and DTPR-4Cl, respectively, which corresponds to the HOMO-LUMO excitation. The red-shifted absorption of CPDT-4Cl and DTPR-4Cl is attributed to the stronger ICT effects, which is supported by the larger dipole moments (**Figure S2b**) between the core and the end groups of CPDT-4Cl (12.19 D) and DTPR-4Cl (12.99 D) than that of IDTT-4Cl (9.66 D).

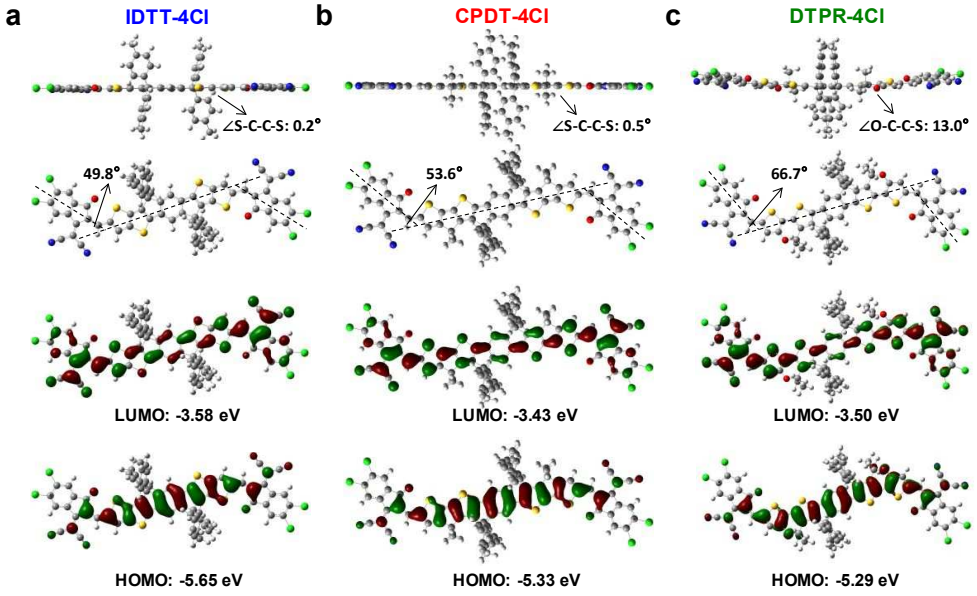

Figure 2. Theoretical calculations of molecular geometry and frontier molecular orbitals for (a) IDTT-4Cl, (b) CPDT-4Cl and (c) DTPR-4Cl. The alkyl chains are replaced with methyl groups to simplify the calculations.

To verify the calculation results, the UV-vis-NIR absorption spectra of three SMAs were recorded in their solution and thin-film state. In diluted chloroform solution (1.0×10^{-6} M), while IDTT-4Cl shows an absorption peak (λ_{max}) centered at 702 nm with a molar extinction coefficient (ε_{max}) of 2.52×10^5 M^{-1} cm^{-1}, dramatically red-shifted absorption peaks together with higher ε_{max} are observed for both CPDT-4Cl (λ_{max} = 804 nm, $\varepsilon_{max} = 3.36\times10^5$ M^{-1} cm^{-1}) and DTPR-4Cl (λ_{max} = 833 nm, $\varepsilon_{max} = 3.00\times10^5$ M^{-1} cm^{-1}), which is in agreement with the TDDFT calculation results. Similarly, in thin-film state, the absorption onsets are extended from 832 nm for IDTT-4Cl to 919 nm for CPDT-4Cl, and to 950 nm for DTPR-4Cl. As a result, the optical bandgap (E_g) of CPDT-4Cl and DTPR-4Cl are determined to be 1.35 and 1.30 eV, respectively, which are greatly reduced compared with IDTT-4Cl (1.49 eV). The smaller E_g of CPDT-4Cl and DTPR-4Cl can be attributed to two factors: the electron-rich cores and extended conjugation lengths. While IDTT-4Cl has a large part of overlapped absorption to the donor polymer PTB7-Th, CPDT-4Cl and DTPR-4Cl can form more complementary absorption in the blends (**Figure S3**). As the photons in the NIR region can be effectively harvested by CPDT-4Cl and DTPR-4Cl, the J_{SC} of the devices are expected to improve. In addition, cyclic voltammetry (CV) was employed to investigate the electrochemical properties of three SMAs in thin-film state (**Figure 3c**). The HOMO and LUMO levels were extracted from the onset oxidation and reduction potentials of the CV curves with the ferrocene/ferrocenium as the external standard, and the results are summarized in **Figure 3d** and **Table 1**. Both CPDT-4Cl (HOMO/LUMO = -5.32/-3.78 eV) and DTPR-4Cl (HOMO/LUMO = -5.35/-3.85 eV) have upshifted energy levels relative to IDTT-4Cl (HOMO/LUMO = -5.49/-3.91 eV), which is consistent with the calculated values shown in **Figure 2**. Therefore, when combined with PTB7-Th, the devices based on CPDT-4Cl and DTPR-4Cl should benefit from higher V_{OC}.

Table 1. Thermal, optical and electrochemical properties of IDTT-4Cl, CPDT-4Cl and DTPR-4Cl.

Material	T_d [°C]	$\lambda_{max,sol}$ [nm]	$\varepsilon_{max,sol}$ [M^{-1} cm^{-1}]	$\lambda_{onset,film}$ [nm]	E_g^{opt} a) [eV]	HOMO/LUMO[a)] [eV]	E_g^{CV} c) [eV]
IDTT-4Cl	375	702	2.52×10^5	832	1.49	-5.49/-3.91	1.58
CPDT-4Cl	383	804	3.36×10^5	919	1.35	-5.32/-3.78	1.54
DTPR-4Cl	353	833	3.00×10^5	950	1.30	-5.35/-3.85	1.50

a) Calculated by $E_g^{opt} = 1240/\lambda_{onset,film}$; b) Estimated from the onset oxidation and reduction potential of the CV curve; c) calculated by E_g^{CV} = LUMO-HOMO.

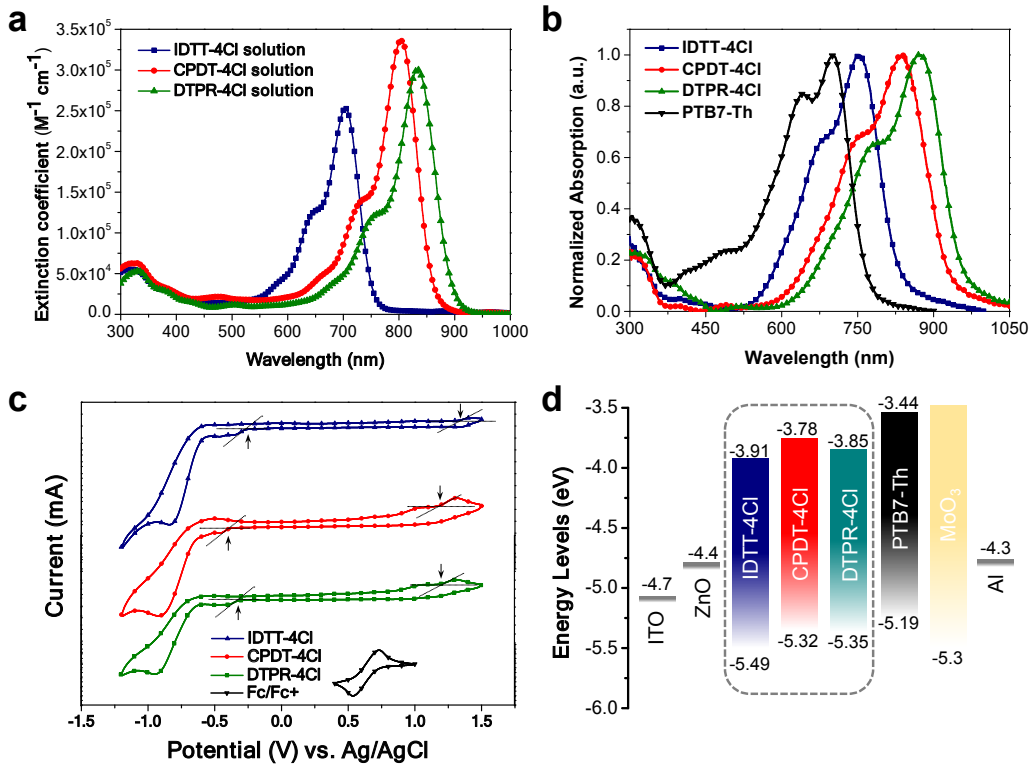

Figure 3. (a) UV-Vis absorption spectra of IDTT-4Cl, CPDT-4Cl and DTPR-4Cl in diluted chloroform solution (concentration: 1.0×10^{-6} M). (b) UV-Vis absorption spectra of PTB7-Th, IDTT-4Cl, CPDT-4Cl and DTPR-4Cl in thin-film state. (c) Cyclic voltammetry curves of IDTT-4Cl, CPDT-4Cl and DTPR-4Cl. (d) Architecture and energy alignment of the bulk heterojunction devices.

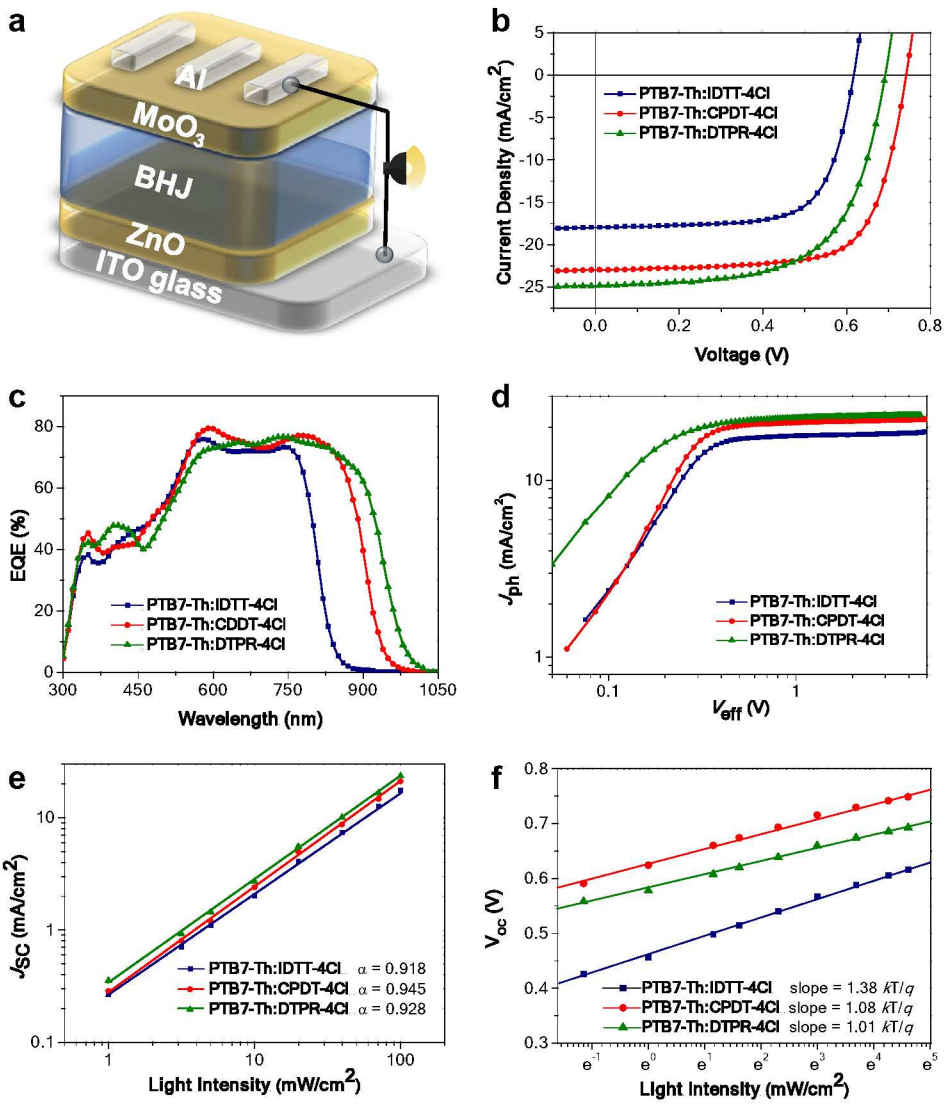

Figure 4. (a) Inverted device structure, (b) *J*-*V* characteristics, (c) EQE curves, (d) photocurrent versus effective voltage plots, (e) light-intensity-dependent J_{SC} experiments and (f) light-intensity-dependent V_{OC} experiments of the PTB7-Th:IDTT-4Cl, PTB7-Th:CPDT-4Cl and PTB7-Th:DTPR-4Cl devices.

To compare the photovoltaic performances of three SMAs, inverted OSC devices with a structure of indium tin oxide (ITO)/ZnO/active layer/MoO3/Al were fabricated. The well-known PTB7-Th was selected as the donor polymer due to its high-lying HOMO level that ensured efficient hole transfer from the SMAs. The details in device

fabrication and optimization are summarized in the Supporting Information, and the device data are collected in **Table 2**. As depicted in **Figure 4a**, the optimal PTB7-Th:IDTT-4Cl devices exhibited an average PCE of 7.16% with a low V_{OC} of 0.61 V, a J_{SC} of 18.34 mA cm^{-2} and a moderate FF of 64.3%. Surprisingly, the optimal PTB7-Th:CPDT-4Cl devices showed a much higher PCE of 12.15% with simultaneously improved V_{OC} of 0.74 V, J_{SC} of 23.24 mA cm^{-2} and FF of 69.1%. The 0.13 V higher V_{OC} of the PTB7-Th:CPDT-4Cl devices can be attributed to the up-shifted energy levels of CPDT-4Cl relative to IDTT-4Cl, as discussed in the electrochemical part. In addition, the stronger absorption as well as broadened absorption range of CPDT-4Cl can explain the better J_{SC} of the devices. However, although the even more red-shifted absorption of DTPR-4Cl compared to CPDT-4Cl resulted in a higher J_{SC} of 24.97 mA cm^{-2}, a FF of 61.8% and a slightly lower V_{OC} of 0.68 V yielded only a moderate PCE of 10.75%.

The external quantum efficiency (EQE) spectra of the three devices are presented in **Figure 4b**. The PTB7-Th:IDTT-4Cl device showed a photon response in the range of 300-800 nm with the peak EQE of 76% at 580 nm. Both CPDT-4Cl and DTPR-4Cl-based devices exhibited dramatically broadened response range to beyond 900 nm, which is consistent with their corresponding absorption range. Moreover, the PTB7-Th:CPDT-4Cl and the PTB7-Th:DTPR-4Cl devices showed higher EQE values of 79% at 590 nm and 77% at 740 nm, respectively. The integrated J_{SC} from EQE curves were calculated to be 17.97, 22.67 and 24.80 mA cm^{-2} for IDTT-4Cl, CPDT-4Cl and DTPR-4Cl-based devices, respectively, which are in good agreement with the values from the *J-V* curves. As a result, the broader photon response range together with the higher EQE values can well explain the improvement of the J_{SC} of devices of the CPDT-4Cl and DTPR-4Cl-based devices. Furthermore, the plots of photocurrent (J_{ph}, defined as J_L - J_D, where J_L and J_D are the current densities under illumination and in the dark, respectively) versus effective voltage (V_{eff}, defined as V - V_0, where V is the applied voltage and V_0 is the voltage at J_{ph} = 0) of the three devices are shown in **Figure 4d**. All the three devices reached their saturated photocurrent density (J_{sat}) at V_{eff} of > 2 V,

suggesting all excitons were dissociated and free charge carriers were completely collected by the electrodes. Besides, the charge dissociation probability (P_{diss}, defined as J_{SC}/J_{sat}) were determined to be 97%, 99% and 99% for the IDTT-4Cl, CPDT-4Cl and DTPR-4Cl-based devices, respectively. The high P_{diss} values are also supported by the high photoluminescence quenching efficiencies of the three blends (94%, 93% and 98% for the IDTT-4Cl, CPDT-4Cl and DTPR-4Cl-based devices, respectively) relative to the pristine PTB7-Th film excited at 633 nm, implying the efficient charge dissociation process (**Figure S4**).

Table 2. Photovoltaic parameters of the inverted devices of IDTT-4Cl, CPDT-4Cl and DTPR-4Cl blended with PTB7-Th under illumination of 100 mW/cm^2.

Material combinations	V_{OC} (V)	J_{SC} (mA cm^{-2})	FF (%)	PCE[a] (%)	PCE_{max} (%)
PTB7-Th:IDTT-4Cl	0.61±0.01	18.34±0.46	64.3±0.1	7.16±0.22	7.70
PTB7-Th:CPDT-4Cl	0.74±0.01	23.24±0.47	69.1±0.2	11.88±0.13	12.15
PTB7-Th:DTPR-4Cl	0.68±0.01	24.97±0.21	61.8±0.1	10.49±0.19	10.75

[a] Average values from 15 devices.

To gain more insights into the origins of the improved photovoltaic performances of the CPDT-4Cl and DTPR-4Cl-based devices, we conducted light-intensity dependent experiments to investigate the charge dissociation and recombination processes. **Figure 4e** presented the relationship between J_{SC} and light intensity described as $J_{SC} \propto P^{\alpha}$, where α is equal to unity when all separated charge carriers are efficiently collected by the corresponding electrodes without recombination. The slopes α were fitted to be 0.918, 0.945 and 0.928 for the IDTT-4Cl, CPDT-4Cl and DTPR-4Cl-based devices, respectively. The largest α of the CPDT-4Cl-based device suggests suppressed bimolecular recombination, which accounts for its FF of ~70%. In addition, the light-intensity-dependent V_{OC} plots of the three devices are also illustrated in **Figure 4f**. A

stronger light-intensity dependence of V_{OC} with a slope of larger than kT/q can be found (where k is the Boltzmann constant, T is the absolute temperature and q is the elementary charge), if more monomolecular recombination occurs, either from the trap-assisted SRH or the geminate recombination. The slopes extracted from the plots are 1.38 kT/q,1.08 kT/q and 1.01 kT/q for the IDTT-4Cl, CPDT-4Cl and DTPR-4Cl-based devices, respectively. Therefore, both light-intensity-dependent J_{SC} and V_{OC} experiments suggest efficiently suppressed recombination for the CPDT-4Cl-based device.

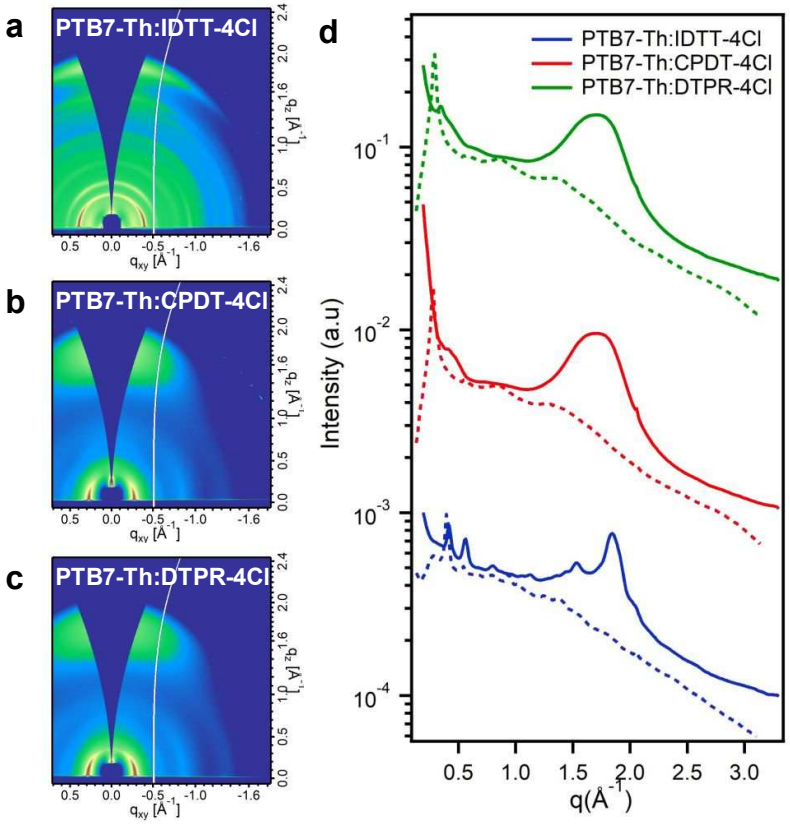

Figure 5. 2D GIWAXS pattern of (a) PTB7-Th:IDTT-4Cl, (b) PTB7-Th:CPDT-4Cl and (c) PTB7-Th:DTPR-4Cl. (d) 1D GIWAXS profiles of the in-plane (dashed lines) and out-of-plane (solid lines) directions.

Grazing-incidence wide-angle X-ray scattering (GIWAXS) was employed to obtain the

detailed information of molecular packing induced by the introduction of the CPDT and DTPR units into the molecular backbone. The two-dimensional GIWAXS patterns of the three blend films are shown in **Figure 5a-c**, and the 1D profiles are plotted in **Figure 5d**. The PTB7-Th:IDTT-4Cl film exhibits a number of sharp and pronounced lamellar and π-π stacking peaks, which should be attributed to the high crystallinity of IDTT-4Cl. The π-π stacking peak locates at q = 1.85 Å^{-1} in the out-of-plane direction, corresponding to a π-π stacking distance (d_{010}) of 3.39 Å and a coherence length (CL_{010}) of 37.8 Å for IDTT-4Cl. In sharp contrast, the CPDT-4Cl-based blend exhibits a lamellar stacking peak located at $q \approx 0.26$ Å^{-1} in the in-plane direction and a broad π-π peak located at $q \approx 1.70$ Å^{-1} (d_{010} = 3.69 Å and CL_{010} = 13.4 Å). Similar to CPDT-4Cl, a broad π-π peak can be observed at $q \approx 1.71$ Å^{-1} for DTPR-4Cl-based devices, which is associated with a d_{010} of 3.67 Å and a CL_{010} of 13.2 Å. The reduction in crystallinity of CPDT-4Cl and DTPR-4Cl can be attributed to the extra propyl chains attached to the molecular backbone, which hinder the excessive intermolecular stacking of end groups and render better solubility of the SMAs with extended conjugation length. Several recent reports also demonstrated that lowering the degree of crystallization for certain highly crystalline SMAs with similar chemical structures to CPDT-4Cl and DTPR-4Cl helps to achieve better morphological compatibility with the donor polymers.[49-51]

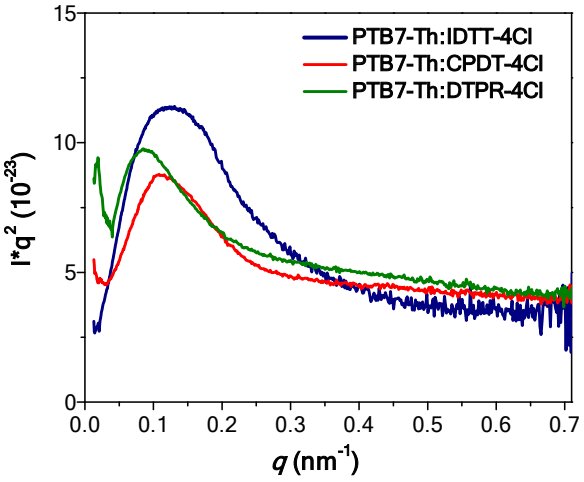

Figure 6. Lorentz-corrected RSoXS profiles of the PTB7-Th:IDTT-4Cl, PTB7-Th:CPDT-4Cl and PTB7-Th:DTPR-4Cl blend films acquired at 283.4 eV.

Resonant soft X-ray scattering (RSoXS) measurements were conducted to investigate the phase separation between PTB7-Th and three SMAs. The Lorentz-corrected RSoXS profiles of the three blend films acquired at 283.4 eV are illustrated in **Figure 6**. It can be observed that the RSoXS profile of the PTB7-Th:DTPR-4Cl blend shifts towards a lower *q* relative to the PTB7-Th:IDTT-4Cl, PTB7-Th:CPDT-4Cl ones. The long period of the blend films are extracted to be 53.9, 55.9 and 72.2 nm for PTB7-Th:IDTT-4Cl, PTB7-Th:CPDT-4Cl and PTB7-Th:DTPR-4Cl, respectively (**Table 3**). In addition, although CPDT-4Cl and DTPR-4Cl show less crystallinity than IDTT-4Cl, they can still achieve comparable root-mean-square composition variation (representing the average phase purity) when blending with PTB7-Th. The difference in phase separation of the blend films are more discernible from their atomic force microscopy (AFM) images. As shown in **Figure S5**, the phase separation of the PTB7-Th:DTPR-4Cl blend is significantly larger than those of the other two blends, which is in agreement with the RSoXS results above. The surface roughness with root-mean-square (RMS) values are derived to be 1.69, 2.75 and 4.55 nm for PTB7-Th:IDTT-4Cl, PTB7-Th:CPDT-4Cl and PTB7-Th:DTPR-4Cl, respectively. Therefore, the relatively low FF of the PTB7-Th:DTPR-4Cl devices can be attributed to the rough surface morphology as well as the excessively large phase separation.

Table 3. Summary of morphological data based on thePTB7-Th:IDTT-4Cl, PTB7-Th:CPDT-4Cl and PTB7-Th:DTPR-4Cl blend.

Material Combinations	d_{010} **(SMA)** (Å)	CL_{010} **(SMA)** (Å)	**Long period** (nm)	**Root-mean-square composition variation**	**χ**
PTB7-Th:IDTT-4Cl	3.39	37.8	53.9	1	0.83
PTB7-Th:CPDT-4Cl	3.69	13.4	55.9	0.94	0.95
PTB7-Th:DTPR-4Cl	3.67	13.2	72.2	0.99	1.02

To better understand the morphological compatibility between PTB7-Th and the three SMAs, contact angle measurements were performed based on the two-solvent method. The surface tensions (γ) of the pristine materials smooth pristine films of PTB7-Th, IDTT-4Cl, CPDT-4Cl and DTPR-4Cl were determined by the Owens-Wendt geometric mean equation utilizing water and ethylene glycol (EG) as solvents (**Figure S6**). The results are collected in **Table S1** and the calculation details are summarized in the Supporting Information.[52] Then, the Flory–Huggins parameter χ were calculated to be 0.83, 0.95 and 1.02 for the PTB7-Th:IDTT-4Cl, PTB7-Th:CPDT-4Cl and PTB7-Th:DTPR-4Cl pair, respectively. The trend in the χ values between PTB7-Th and three SMAs is well consistent with that in the RSoXS and AFM measurement, as a larger χ value would induce stronger phase separation and larger domain sizes. The largest χ between PTB7-Th and DTPR-4Cl results in excessively large domains, while the moderate χ between PTB7-Th and CPDT-4Cl leads to suitable miscibility and phase separation.

3. Conclusions

In conclusion, two low-bandgap SMAs named CPDT-4Cl and DTPR-4Cl with absorption onset of beyond 900 nm were constructed by incorporating strong electron-donating building blocks (CPDT and DTPR) into the molecular backbones. Compared with IDTT-4Cl, the enhanced ICT effects of CPDT-4Cl and DTPR-4Cl led to dramatically red-shifted absorption and up-shifted HOMO levels, as evidenced by theoretical calculations as well as optical and electrochemical measurements. When blending with PTB7-Th as the donor, the CPDT-4Cl and DTPR-4Cl-based devices showed improved J_{SC} of 23.24 and 24.97 mA cm^{-2}, respectively, owing to their extended absorption range relative to the IDTT-4Cl ones. In addition, the PTB7-Th:CPDT-4Cl blend exhibited suitable phase separation as demonstrated by the AFM and surface tension experiments, resulting in suppressed charge recombination and a high FF of ~70%. Consequently, a high PCE of 12.15% was achieved by the PTB7-Th:CPDT-4Cl device, which outperformed that of the PTB7-Th:IDTT-4Cl one (7.70%).

Although the PTB7-Th:DTPR-4Cl device yielded only a moderate PCE of 10.75%, the most red-shifted absorption of DTPR-4Cl still demonstrates the potential applications of the DTPR building block in the design of low-bandgap SMAs. Overall, this work highlights the great potential of the electron-donating CPDT and DTPR units as promising building blocks to construct high-performance low-bandgap SMAs.

Conflicts of interest

The authors declare no competing financial interest.

Author Contributions

‡ J. Z., Y. L. and Z. P. contributed equally to this work.

Acknowledgements

The work described in this paper was partially supported by the Shen Zhen Technology and Innovation Commission (project number JCYJ20170413173814007, JCYJ20170818113905024), the Hong Kong Research Grants Council (Research Impact Fund R6021-18, project numbers 16305915, 16322416, 606012, and 16303917) and Hong Kong Innovation and Technology Commission for the support through projects ITC-CNERC14SC01 and ITS/471/18). X-ray data acquisition and manuscript input by NCSU authors supported by ONR grant N000141712204. X-ray data were acquired at the Advanced Light Source, which was supported by the Director, Office of Science, Office of Basic Energy Sciences, of the U.S. Department of Energy under Contract DE-AC02-05CH11231.

Reference

1. J. Q. Zhang, H. S. Tan, X. G. Guo, A. Facchetti and H. Yan, Material insights and challenges for non-fullerene organic solar cells based on small molecular acceptors, *Nat. Energy*, 2018, **3**, 720-731.
2. J. Hou, O. Inganas, R. H. Friend and F. Gao, Organic solar cells based on non-

fullerene acceptors, *Nat. Mater.*, 2018, **17**, 119-128.

3. C. Yan, S. Barlow, Z. Wang, H. Yan, A. K. Y. Jen, S. R. Marder and X. Zhan, Non-fullerene acceptors for organic solar cells, *Nat. Rev. Mater.*, 2018, **3**, 18003.
4. P. Cheng, G. Li, X. W. Zhan and Y. Yang, Next-generation organic photovoltaics based on non-fullerene acceptors, *Nat. Photon.*, 2018, **12**, 131-142.
5. G. Zhang, J. Zhao, P. C. Y. Chow, K. Jiang, J. Zhang, Z. Zhu, J. Zhang, F. Huang and H. Yan, Nonfullerene Acceptor Molecules for Bulk Heterojunction Organic Solar Cells, *Chem. Rev.*, 2018, **118**, 3447-3507.
6. J. Yuan, Y. Zhang, L. Zhou, G. Zhang, H.-L. Yip, T.-K. Lau, X. Lu, C. Zhu, H. Peng, P. A. Johnson, M. Leclerc, Y. Cao, J. Ulanski, Y. Li and Y. Zou, Single-Junction Organic Solar Cell with over 15% Efficiency Using Fused-Ring Acceptor with Electron-Deficient Core, *Joule*, 2019, **3**, 1140–1151.
7. L. Hong, H. Yao, Z. Wu, Y. Cui, T. Zhang, Y. Xu, R. Yu, Q. Liao, B. Gao, K. Xian, H. Y. Woo, Z. Ge and J. Hou, Eco-Compatible Solvent-Processed Organic Photovoltaic Cells with Over 16% Efficiency, *Adv. Mater.*, 2019, **31**, 1903441.
8. J. Yuan, T. Huang, P. Cheng, Y. Zou, H. Zhang, J. L. Yang, S. Y. Chang, Z. Zhang, W. Huang, R. Wang, D. Meng, F. Gao and Y. Yang, Enabling low voltage losses and high photocurrent in fullerene-free organic photovoltaics, *Nat. Commun.*, 2019, **10**, 570.
9. H. Sun, T. Liu, J. Yu, T.-K. Lau, G. Zhang, Y. Zhang, M. Su, Y. Tang, R. Ma, B. Liu, J. Liang, K. Feng, X. Lu, X. Guo, F. Gao and H. Yan, A monothiophene unit incorporating both fluoro and ester substitution enabling high-performance donor polymers for non-fullerene solar cells with 16.4% efficiency, *Energy Environ. Sci.*, 2019, **12**, 3328-3337.
10. H. Zhang, H. Yao, J. Hou, J. Zhu, J. Zhang, W. Li, R. Yu, B. Gao, S. Zhang and J. Hou, Over 14% Efficiency in Organic Solar Cells Enabled by Chlorinated Nonfullerene Small-Molecule Acceptors, *Adv. Mater.*, 2018, **30**, 1800613.

11. S. Zhang, Y. Qin, J. Zhu and J. Hou, Over 14% Efficiency in Polymer Solar Cells Enabled by a Chlorinated Polymer Donor, *Adv. Mater.*, 2018, **30**, 1800868.
12. S. Li, L. Ye, W. Zhao, H. Yan, B. Yang, D. Liu, W. Li, H. Ade and J. Hou, A Wide Band Gap Polymer with a Deep Highest Occupied Molecular Orbital Level Enables 14.2% Efficiency in Polymer Solar Cells, *J. Am. Chem. Soc.*, 2018, **140**, 7159-7167.
13. H. Yao, Y. Cui, D. Qian, C. S. Ponseca, Jr., A. Honarfar, Y. Xu, J. Xin, Z. Chen, L. Hong, B. Gao, R. Yu, Y. Zu, W. Ma, P. Chabera, T. Pullerits, A. Yartsev, F. Gao and J. Hou, 14.7% Efficiency Organic Photovoltaic Cells Enabled by Active Materials with a Large Electrostatic Potential Difference, *J. Am. Chem. Soc.*, 2019, **141**, 7743-7750.
14. Y. Lin, J. Wang, Z. G. Zhang, H. Bai, Y. Li, D. Zhu and X. Zhan, An electron acceptor challenging fullerenes for efficient polymer solar cells, *Adv. Mater.*, 2015, **27**, 1170-1174.
15. Y. Lin, F. Zhao, Q. He, L. Huo, Y. Wu, T. C. Parker, W. Ma, Y. Sun, C. Wang, D. Zhu, A. J. Heeger, S. R. Marder and X. Zhan, High-Performance Electron Acceptor with Thienyl Side Chains for Organic Photovoltaics, *J. Am. Chem. Soc.*, 2016, **138**, 4955-4961.
16. Y. Yang, Z. G. Zhang, H. Bin, S. Chen, L. Gao, L. Xue, C. Yang and Y. Li, Side-Chain Isomerization on an n-type Organic Semiconductor ITIC Acceptor Makes 11.77% High Efficiency Polymer Solar Cells, *J. Am. Chem. Soc.*, 2016, **138**, 15011-15018.
17. S. Li, L. Ye, W. Zhao, S. Zhang, S. Mukherjee, H. Ade and J. Hou, Energy-Level Modulation of Small-Molecule Electron Acceptors to Achieve over 12% Efficiency in Polymer Solar Cells, *Adv. Mater.*, 2016, **28**, 9423-9429.
18. W. Zhao, S. Li, H. Yao, S. Zhang, Y. Zhang, B. Yang and J. Hou, Molecular Optimization Enables over 13% Efficiency in Organic Solar Cells, *J. Am. Chem. Soc.*, 2017, **139**, 7148-7151.
19. Y. Cui, C. Yang, H. Yao, J. Zhu, Y. Wang, G. Jia, F. Gao and J. Hou, Efficient

Semitransparent Organic Solar Cells with Tunable Color enabled by an Ultralow-Bandgap Nonfullerene Acceptor, *Adv. Mater.*, 2017, **29**, 1703080.

20. H. Yao, L. Ye, J. Hou, B. Jang, G. Han, Y. Cui, G. M. Su, C. Wang, B. Gao, R. Yu, H. Zhang, Y. Yi, H. Y. Woo, H. Ade and J. Hou, Achieving Highly Efficient Nonfullerene Organic Solar Cells with Improved Intermolecular Interaction and Open-Circuit Voltage, *Adv. Mater.*, 2017, **29**, 1700254.
21. Y. Z. Chen, T. Liu, H. W. Hu, T. X. Ma, J. Y. L. Lai, J. Q. Zhang, H. Ade and H. Yan, Modulation of End Groups for Low-Bandgap Nonfullerene Acceptors Enabling High-Performance Organic Solar Cells, *Adv. Energy Mater.*, 2018, **8**, 1801203.
22. J. Zhang, G. Xu, F. Tao, G. Zeng, M. Zhang, Y. M. Yang, Y. Li and Y. Li, Highly Efficient Semitransparent Organic Solar Cells with Color Rendering Index Approaching 100, *Adv. Mater.*, 2019, **31**, 1807159.
23. Y. Li, J. D. Lin, X. Che, Y. Qu, F. Liu, L. S. Liao and S. R. Forrest, High Efficiency Near-Infrared and Semitransparent Non-Fullerene Acceptor Organic Photovoltaic Cells, *J. Am. Chem. Soc.*, 2017, **139**, 17114-17119.
24. L. Meng, Y. Zhang, X. Wan, C. Li, X. Zhang, Y. Wang, X. Ke, Z. Xiao, L. Ding, R. Xia, H. L. Yip, Y. Cao and Y. Chen, Organic and solution-processed tandem solar cells with 17.3% efficiency, *Science*, 2018, **361**, 1094-1098.
25. L. Zuo, J. Yu, X. Shi, F. Lin, W. Tang and A. K. Jen, High-Efficiency Nonfullerene Organic Solar Cells with a Parallel Tandem Configuration, *Adv. Mater.*, 2017, **29**, 1702547.
26. X. Z. Che, Y. X. Li, Y. Qu and S. R. Forrest, High fabrication yield organic tandem photovoltaics combining vacuum- and solution-processed subcells with 15% efficiency, *Nat. Energy*, 2018, **3**, 422-427.
27. Q. Liao, H. Sun, B. Li and X. Guo, 26 mA cm−2 JSC achieved in the integrated solar cells, *Sci. Bull.*, 2019, **64**, 1747-1749.
28. R. N. Yu, H. F. Yao and J. H. Hou, Recent Progress in Ternary Organic Solar Cells Based on Nonfullerene Acceptors, *Adv. Energy Mater.*, 2018, **8**, 1702814.

29. N. Gasparini, A. Salleo, I. McCulloch and D. Baran, The role of the third component in ternary organic solar cells, *Nat. Rev. Mater.*, 2019, **4**, 229-242.

30. Z. Xiao, X. Jia and L. M. Ding, Ternary organic solar cells offer 14% power conversion efficiency, *Sci. Bull.*, 2017, **62**, 1562-1564.

31. Z. C. Zhou, S. J. Xu, J. N. Song, Y. Z. Jin, Q. H. Yue, Y. H. Qian, F. Liu, F. L. Zhang and X. Z. Zhu, High-efficiency small-molecule ternary solar cells with a hierarchical morphology enabled by synergizing fullerene and non-fullerene acceptors, *Nat. Energy*, 2018, **3**, 952-959.

32. H. Yao, Y. Chen, Y. Qin, R. Yu, Y. Cui, B. Yang, S. Li, K. Zhang and J. Hou, Design and Synthesis of a Low Bandgap Small Molecule Acceptor for Efficient Polymer Solar Cells, *Adv. Mater.*, 2016, **28**, 8283-8287.

33. J. Sun, X. Ma, Z. Zhang, J. Yu, J. Zhou, X. Yin, L. Yang, R. Geng, R. Zhu, F. Zhang and W. Tang, Dithieno[3,2-b:2',3'-d]pyrrol Fused Nonfullerene Acceptors Enabling Over 13% Efficiency for Organic Solar Cells, *Adv. Mater.*, 2018, **30**, 1707150.

34. H. Yao, Y. Cui, R. Yu, B. Gao, H. Zhang and J. Hou, Design, Synthesis, and Photovoltaic Characterization of a Small Molecular Acceptor with an Ultra-Narrow Band Gap, *Angew. Chem. Int. Ed.*, 2017, **56**, 3045-3049.

35. Z. Xiao, X. Jia, D. Li, S. Wang, X. Geng, F. Liu, J. Chen, S. Yang, T. P. Russell and L. Ding, 26 mA cm−2 Jsc from organic solar cells with a low-bandgap nonfullerene acceptor, *Sci. Bull.*, 2017, **62**, 1494-1496.

36. D. X. Liu, T. Wang, X. Ke, N. Zheng, Z. T. Chang, Z. Q. Xie and Y. S. Liu, Ultra-narrow bandgap non-fullerene acceptors for organic solar cells with low energy loss, *Mater. Chem. Front.*, 2019, **3**, 2157-2163.

37. S. Dai, T. Li, W. Wang, Y. Xiao, T. K. Lau, Z. Li, K. Liu, X. Lu and X. Zhan, Enhancing the Performance of Polymer Solar Cells via Core Engineering of NIR-Absorbing Electron Acceptors, *Adv. Mater.*, 2018, **30**, 1706571.

38. Z. Yao, X. Liao, K. Gao, F. Lin, X. Xu, X. Shi, L. Zuo, F. Liu, Y. Chen and A. K. Jen, Dithienopicenocarbazole-Based Acceptors for Efficient Organic Solar

Cells with Optoelectronic Response Over 1000 nm and an Extremely Low Energy Loss, *J. Am. Chem. Soc.*, 2018, **140**, 2054-2057.

39. F. Liu, Z. Zhou, C. Zhang, J. Zhang, Q. Hu, T. Vergote, F. Liu, T. P. Russell and X. Zhu, Efficient Semitransparent Solar Cells with High NIR Responsiveness Enabled by a Small-Bandgap Electron Acceptor, *Adv. Mater.*, 2017, **29**, 1606574.
40. F. X. Chen, J. Q. Xu, Z. X. Liu, M. Chen, R. Xia, Y. Yang, T. K. Lau, Y. Zhang, X. Lu, H. L. Yip, A. K. Jen, H. Chen and C. Z. Li, Near-Infrared Electron Acceptors with Fluorinated Regioisomeric Backbone for Highly Efficient Polymer Solar Cells, *Adv. Mater.*, 2018, **30**, 1803769.
41. W. Wang, C. Yan, T. K. Lau, J. Wang, K. Liu, Y. Fan, X. Lu and X. Zhan, Fused Hexacyclic Nonfullerene Acceptor with Strong Near-Infrared Absorption for Semitransparent Organic Solar Cells with 9.77% Efficiency, *Adv. Mater.*, 2017, **29**, 1701308.
42. L. Dou, Y. Liu, Z. Hong, G. Li and Y. Yang, Low-Bandgap Near-IR Conjugated Polymers/Molecules for Organic Electronics, *Chem. Rev.*, 2015, **115**, 12633-12665.
43. L. Dou, C.-C. Chen, K. Yoshimura, K. Ohya, W.-H. Chang, J. Gao, Y. Liu, E. Richard and Y. Yang, Synthesis of 5H-Dithieno[3,2-b:2′,3′-d]pyran as an Electron-Rich Building Block for Donor–Acceptor Type Low-Bandgap Polymers, *Macromolecules*, 2013, **46**, 3384-3390.
44. M. Wang, H. Wang, T. Yokoyama, X. Liu, Y. Huang, Y. Zhang, T. Q. Nguyen, S. Aramaki and G. C. Bazan, High open circuit voltage in regioregular narrow band gap polymer solar cells, *J. Am. Chem. Soc.*, 2014, **136**, 12576-12579.
45. J. You, L. Dou, K. Yoshimura, T. Kato, K. Ohya, T. Moriarty, K. Emery, C. C. Chen, J. Gao, G. Li and Y. Yang, A polymer tandem solar cell with 10.6% power conversion efficiency, *Nat Commun*, 2013, **4**, 1446.
46. Q. He, M. Shahid, J. Wu, X. Jiao, F. D. Eisner, T. Hodsden, Z. Fei, T. D. Anthopoulos, C. R. McNeill, J. R. Durrant and M. Heeney, Fused

Cyclopentadithienothiophene Acceptor Enables Ultrahigh Short-Circuit Current and High Efficiency >11% in As-Cast Organic Solar Cells, *Adv. Funct. Mater.*, 2019, **29**, 1904956.

47. Y. Q. Q. Yi, H. R. Feng, X. Ke, J. Yan, M. J. Chang, X. J. Wan, C. X. Li and Y. S. Chen, A cyclopentadithiophene-bridged small molecule acceptor with near-infrared light absorption for efficient organic solar cells, *J. Mater. Chem. C*, 2019, **7**, 4013-4019.
48. Y. Q. Q. Yi, H. R. Feng, N. Zheng, X. Ke, B. Kan, M. J. Chang, Z. Q. Xie, X. J. Wan, C. X. Li and Y. S. Chen, Small Molecule Acceptors with a Nonfused Architecture for High-Performance Organic Photovoltaics, *Chem. Mater.*, 2019, **31**, 904-911.
49. S. Dai, F. Zhao, Q. Zhang, T. K. Lau, T. Li, K. Liu, Q. Ling, C. Wang, X. Lu, W. You and X. Zhan, Fused Nonacyclic Electron Acceptors for Efficient Polymer Solar Cells, *J. Am. Chem. Soc.*, 2017, **139**, 1336-1343.
50. W. Li, M. Chen, J. Cai, E. L. Spooner, H. Zhang, R. S. Gurney, D. Liu, Z. Xiao, D. G. Lidzey and L. Ding, Molecular order control of non-fullerene acceptors for high-efficiency polymer solar cells, *Joule*, 2019, **3**, 819-833.
51. W. Li, M. Chen, Z. Zhang, J. Cai, H. Zhang, R. S. Gurney, D. Liu, J. Yu, W. Tang and T. Wang, Retarding the Crystallization of a Nonfullerene Electron Acceptor for High-Performance Polymer Solar Cells, *Adv. Funct. Mater.*, 2018, **29**, 1807662.
52. S. Kouijzer, J. J. Michels, M. van den Berg, V. S. Gevaerts, M. Turbiez, M. M. Wienk and R. A. Janssen, Predicting morphologies of solution processed polymer:fullerene blends, *J. Am. Chem. Soc.*, 2013, **135**, 12057-12067.